Investigation of $^{16}O + {}^{16}O$ elastic scattering using the α-cluster folding model

M. A. Hassanain,[1,2] Awad A. Ibraheem,[1,3] Shikha M. M. Al Sebiey,[1] S. R. Mokhtar,[4] M. A. Zaki,[5] Zakaria M. M. Mahmoud,[2] K. O. Behairy,[5] and M. El-Azab Farid[4]

[1]*Department of Physics, King Khalid University, Abha, Saudia Arabia*

[2]*Department of Physics, New-Valley Faculty of Education, El-Kharga, Assiut University, Egypt*

[3]*Department of Physics, Al-Azhar University, Assiut Branch, Assiut, Egypt*

[4]*Department of Physics, Assiut University, Assiut 71516, Assiut, Egypt*

[5]*Department of Physics, Aswan University, Aswan, Egypt*

(Received 6 February 2013; revised manuscript received 7 March 2013; published 13 June 2013)

Angular distributions of $^{16}O + {}^{16}O$ elastic scattering at energies that range from 124 to 1120 MeV have been analyzed in the framework of the double folding (DF) optical model. Based upon the α-cluster structure of the ^{16}O nucleus, two different versions of the real DF optical potential have been generated by using three effective α-α, α-nucleon (N) and nucleon-nucleon (NN) interactions. A microscopic optical potential built upon the M3Y effective NN interaction and the matter density distribution of the ^{16}O nucleus has also been extracted. The obtained real potentials, in conjunction with phenomenological squared Woods-Saxon imaginary parts, have successfully reproduced seven sets of elastic-scattering data. No renormalization of the real folded α-cluster potentials is required to fit the data. The energy dependence of the extracted real and imaginary volume integrals and total reaction cross section has also been investigated.

DOI: 10.1103/PhysRevC.87.064606 PACS number(s): 24.10.Ht, 25.70.Bc, 24.50.+g, 21.60.Gx

I. INTRODUCTION

The refractive (rainbow) structure observed in nucleus-nucleus elastic scattering can provide information on the heavy-ion (HI) optical potential at short internuclear distances. The rainbow phenomenon has been found in several experiments [1–3] on light HI systems, such as $^{12}C + {}^{12}C$, $^{12}C + {}^{16}O$, and $^{16}O + {}^{16}O$. Some attempts [4,5] were carried out to modify the M3Y effective nucleon-nucleon (NN) interaction [6] by introducing an explicit density dependence to account for the in-medium effects that are more substantial at internuclear distances. This modification generated the so-called DDM3Y effective interaction. New precise and complete data for the $^{16}O + {}^{16}O$ interaction revealed a very clear sensitivity of large-angle scattering to the details of the real potential at short distances at which there are large density overlaps of the colliding nuclei. In this situation, the double folding (DF) potential reveals a pronounced sensitivity to the details of the considered effective nucleon-nucleon interaction [7–9], and it has been shown that a consistent description can only be obtained with distinct but small density dependence [7–10].

Khoa *et al.* [11] used different density-dependent versions of the M3Y effective NN interaction for analyses of the refractive structure in the elastic scattering of the α nucleus, $^{12}C + {}^{12}C$, and $^{16}O + {}^{16}O$ data. Nicoli *et al.* [12] have measured and have analyzed the elastic scattering of $^{16}O + {}^{16}O$ at nine energies between 75 and 124 MeV by using the phenomenological and folding model potentials. It was found [11,12] that the real part of the optical potential slightly varies with energy over the studied energy range. The shape of the imaginary part, however, rapidly changes with increasing energy higher than 90 MeV. Nonetheless, the energy dependence of the volume integral of the real and imaginary parts is in agreement with the dispersion relation predictions. In addition, Khoa *et al.* [13] have performed a detailed optical model (OM) analysis of the whole data set in the energy range of 124–1120 MeV to study the evolution of the refractive structure with increasing incident energy by using both the phenomenological squared Woods-Saxon (WS2) and the microscopic DF potentials. Over a wide energy range from 7 to 70 MeV/nucleon, the $^{16}O + {}^{16}O$ scattering system has been studied by Oertzen *et al.* [14]. They obtained excellent fits with data at all considered energies by using deep real DF potentials that involved a NN interaction weakly dependent on the density. In a more recent study, Khoa *et al.* [15] measured and analyzed the data of inelastic $^{16}O + {}^{16}O$ scattering to the lowest 2^+ and 3^- excited states of ^{16}O through the energy range of 250–1120 MeV by using the inelastic form factor extracted by the DF model.

On the other hand, the folding approach has been employed in the framework of the α-cluster model [16,17] to extract a semimicroscopic description of the α-nucleus and nucleus-nucleus potentials. These potentials have proved to give a good description of light HI elastic-scattering data [18–21]. In this context, El-Azab Farid *et al.* [19], El-Azad Farid [20], Karakoc and co-workers [21], and Kurkcuoglu *et al.* [22] have generated α-particle single folding cluster (SFC) and light HI double folding cluster (DFC) optical potentials based upon an appropriate α-α effective interaction. They [19–22] assumed that projectile and target nuclei consist of an integral multiple of a number of α particles. However, in some of the studied reactions, it was essential to introduce reducing renormalization coefficients ($\sim$0.7–0.9) to obtain a successful description of the HI elastic-scattering data. Yang and Li [23] calculated the angular distributions of $^{16}O + {}^{16}O$ elastic scattering at incident energies that ranged from 75 to 350 MeV by using the α-folding potential. They concluded that the reason for the decrease in the renormalization factors with increasing energy was the effect of the reduction in the strength of the α-α interaction with an increase in energy.

In the last decade, Abdullah and his collaborators, in three successive articles [24–26], proposed a successful SFC model to describe the differential cross section of the elastic scattering of α particles on ^{12}C, ^{16}O, and ^{40,44,48}Ca targets as well as a DFC one for ^{16}O + ^{12}C scattering over a broad spectrum of incident energies. They [24–26] considered the point of view that, most of the time, a number of nucleons in the target nucleus are primarily in α-like clusters and the rest are in an unclustered nucleonic configuration. They deduced the α-cluster structure configurations for ^{12}C, ^{16}O, and ^{40,44,48}Ca, respectively, as $2.35\alpha + 2.6N$, $3.5\alpha + 2N$, $8.5\alpha + 6N$, $8.5\alpha + 10N$, and $8.5\alpha + 14N$, where N is an integer. Consequently, this leads us to consider the folding potential as a sum of two parts, one convoluted over the α-cluster density distribution and the other over the nucleonic density distribution. In this formalism, no renormalization was required to fit the data.

Recently, Hassanain *et al.* [27] used the same representation as Refs. [24–26], two different versions of the ^{12}C + ^{12}C real DFC optical potential (DFC1 and DFC2), which have been generated based upon effective α-α, α-N, and NN interactions. The elastic-scattering data at the energy range of 70–360 MeV were successfully reproduced by using the derived potentials. No renormalization of the real DFC1and DFC2 potentials was required to fit the data. In addition, in two very recent articles [28,29], Hassanain analyzed the elastic and inelastic ^{12}C + ^{12}C scattering and elastic ^{24}Mg + ^{28}Si scattering, respectively, by using the DFC potential and coupled-channels mechanism. A successful description of the data is obtained over the full measured angular range without the need to normalize the DFC potential. He also investigated the anomaly in large-angle-scattering and rainbow-scattering features.

In the present paper, we extend the α-cluster folding formalism, presented in our previous studies [27–29], to investigate the ^{16}O + ^{16}O elastic scattering in the framework of the two potential models, the DFC1 [19,22] and DFC2 [27–29]. Seven sets of the ^{16}O + ^{16}O elastic-scattering data over the energy range of 124–1120 MeV are analyzed by using the generated DFC potentials. In the following section, we introduce the optical potential model, whereas, the calculations procedure is described in Sec. III. Section IV is devoted to results and discussion, and finally, conclusions are summarized in Sec. V.

II. THE OPTICAL MODEL

Four different forms of the nuclear optical model potential are used in the present calculations to perform a comparative study of the ^{16}O + ^{16}O reaction. First, the phenomenological WS2 form is considered. Then, two forms are calculated based upon phenomenological α-α, α-N, and NN interactions, denoted as DFC1 and DFC2 potentials. Finally, the potential form is microscopically derived by using the realistic effective M3Y interaction. Details of these potential forms are explained in the following subsections.

A. Phenomenological potentials

The ^{16}O + ^{16}O scattering data have been phenomenologically analyzed by many authors by using several representations. In general, for the best fits, this system requires being represented by an imaginary part composed of volume plus surface terms, whereas, the real part has been assumed to have either WS or WS2 form factors. So, in the present paper, we assume, in accordance with previous phenomenological analyses of the ^{16}O + ^{16}O system [11–14,22], the WS2 shape for the real nuclear potential and the sum of the WS2 "volume" term plus a derivative Woods-Saxon (WSD) "surface" term for the imaginary part. The phenomenological nucleus-nucleus potential $U_{ph}(R)$ is then given as

$$U_{ph}(R) = V_C(R) - V_0[f_V(R)]^n - iW_0[f_I(R)]^n - iW_D f_D(R), \quad (1)$$

where the WS form factor is defined as

$$f_x(R) = \left[1 + \exp\left(\frac{R - r_x\left(A_P^{1/3} + A_T^{1/3}\right)}{a_x}\right)\right]^{-1}, \quad (2)$$

where x denotes the real (V) or imaginary volume (I) potentials, r_x and a_x are the radius and diffuseness parameters, respectively, and A_P and A_T are the mass numbers of the projectile and target nuclei, respectively. The WSD term is formed as

$$f_D(R) = -4n \exp\left(\frac{R - r_D\left(A_P^{1/3} + A_T^{1/3}\right)}{a_D}\right) \Big/ \left\{1 + \exp\left[R - r_D\left(A_P^{1/3} + A_T^{1/3}\right)/a_D\right]\right\}^{(n+1)}. \quad (3)$$

In Eq. (1), $n = 1$ and 2 for the WS and WS2 forms, respectively. The Coulomb potential $V_C(R)$, used in our OM analyzes, is generated by folding two uniform charge distributions of radius $R_c = 3.54$ fm, which have a rms charge radius close to that extracted from the electron-scattering data for the ^{16}O nucleus. This choice has been shown to be accurate up to very small internuclear distances where the nuclear interaction becomes dominant [30]. All OM analyses are carried out by using the computer codes HIOPTIM-94 [31] and HERMES [32]. The WS parameters in Eqs. (1)–(3) are adjusted to obtain the least χ^2 fit to the measured elastic-scattering data.

In general, for an interaction potential $U(R)$ between two nuclei that have nucleon numbers A_P and A_T, the volume integral per interacting nucleon pair J_U is defined as

$$J_U = \frac{4\pi}{A_P A_T} \int U(R) R^2 dR. \quad (4)$$

This quantity is currently used as a sensitive measure of the potential strength. In our paper, we apply this definition to the real and to the imaginary parts of $U(R)$, independently denoted as J_R and J_I, respectively.

B. Folding approaches

In parallel to the phenomenological OM analysis, the DF model analysis of the considered (^{16}O + ^{16}O)-scattering system has also been performed by using three different treatments of the folding procedure. In the first, the 4α-cluster structure of the ^{16}O nucleus (^{16}O $\equiv 4\alpha$) is considered. Then, the DF potential is generated by folding an α-α effective interaction with the α-cluster density distributions in both

projectile and target nuclei [19,20,27,29]. If one denotes the density distributions of the α cluster inside the projectile and the target by ρ_{CP} and ρ_{CT}, respectively, the DFC1 potential can be formulated [19,20,27,29] as

$$U_{\rm DFC1}(R) = \iint \rho_{CP}(r_1)\rho_{CT}(r_2)V_{\alpha\text{-}\alpha} \times(|\vec{R} - \vec{r}_1 + \vec{r}_2|)d\vec{r}_1 d\vec{r}_2, \quad (5)$$

where R denotes the projectile-target relative position vector and r_1 and r_2 are the c.m. coordinates of the α clusters in the projectile and target nuclei, respectively. The α-α effective interaction $V_{\alpha\text{-}\alpha}$ is parametrized as [24–27,33]

$$V_{\alpha\text{-}\alpha}(s) = V_R \exp\left(-\mu_R^2 s^2\right) - V_A \exp\left(-\mu_A^2 s^2\right), \quad (6)$$

where V_A and V_R, respectively, are the attractive and repulsive depths and μ_A and μ_R are the corresponding range parameters. We consider $V_A = 122.62$ MeV, $\mu_A = 0.469$, and $\mu_R = 0.54$ fm^{-1} while the depth V_R is kept as a free parameter in the calculations. The α-cluster distribution inside ^{16}O will be described in the next subsection.

To deduce the second folded cluster potential, denoted as DFC2, we consider the cluster structure of the ^{16}O nucleus defined as $^{16}\text{O} \equiv A_\alpha\alpha + A_N N$; i.e., the ^{16}O nucleus is composed of A_α α particles plus A_N unclustered nucleons such that $4A_\alpha + A_N = 16$. Consequently, if one denotes the density distributions of the α clusters and unclustered nucleons in the projectile and target by $\rho_{\alpha P}$, ρ_{NP}, $\rho_{\alpha T}$, and ρ_{NT}, respectively, the DFC2 potential can be constructed as

$$\begin{aligned} U_{\rm DFC2}(R) = &\iint \rho_{\alpha P}(r_{\alpha P})\rho_{\alpha T}(r_{\alpha T})V_{\alpha\text{-}\alpha}(|\vec{R} - \vec{r}_{\alpha P} + \vec{r}_{\alpha T}|)d\vec{r}_{\alpha P}d\vec{r}_{\alpha T} \\ &+ \iint \rho_{\alpha P}(r_{\alpha P})\rho_{NT}(r_{NT})V_{\alpha\text{-}N}(|\vec{R} - \vec{r}_{\alpha P} + \vec{r}_{NT}|)d\vec{r}_{\alpha P}d\vec{r}_{NT} \\ &+ \iint \rho_{\alpha T}(r_{\alpha T})\rho_{NP}(r_{NP})V_{\alpha\text{-}N}(|\vec{R} - \vec{r}_{\alpha T} + \vec{r}_{NP}|)d\vec{r}_{\alpha T}d\vec{r}_{NP} \\ &+ \iint \rho_{NT}(r_{NT})\rho_{NP}(r_{NP})V_{N\text{-}N}(|\vec{R} - \vec{r}_{NT} + \vec{r}_{NP}|)d\vec{r}_{NT}d\vec{r}_{NP}, \end{aligned} \quad (7)$$

where $r_{\alpha P}$ (r_{NP}) and $r_{\alpha T}$ (r_{NT}) , respectively, are the c.m. coordinates of the α clusters (unclustered nucleons) in the projectile and target nuclei, $V_{\alpha\text{-}N}$ and $V_{N\text{-}N}$ are the α-N and NN effective interactions, respectively. The α-N interaction has the following form [34]:

$$V_{\alpha\text{-}N}(s) = -V_{0\alpha N} \exp(-K^2 s^2), \quad (8)$$

with $V_{\alpha\text{-}N} = 47.3$ MeV and $K = 0.435$ fm^{-1}. The NN potential is given in a Gaussian form as [35]

$$V_{N\text{-}N}(s) = -V_{0NN} \exp\left(-\frac{s^2}{a^2}\right), \quad (9)$$

with $V_{0N\text{-}N} = 20.97$ MeV and $a = 1.47$ fm.

The last treatment is based upon the well-known M3Y effective interaction. The DF calculation is carried out by folding the M3Y interaction over the nuclear matter density distributions for projectile and target nuclei (see Fig. 1). So, the M3Y DF potential is defined as

$$V_{\rm M3Y}(R) = \int \rho_P(r_P)\rho_T(r_T)V_{nn}(s)d\vec{r}_P d\vec{r}_T, \quad (10)$$

whereρ_P and ρ_T are the density distributions for projectile and target nuclei, respectively, and V_{nn} is the M3Y effective NN interaction [36], which is given as

$$V_{nn}(s) = 7999\frac{\exp(-4s)}{4s} - 2134\frac{\exp(-2.5s)}{2.5s} + J_{00}\delta(s). \quad (11)$$

The last term in Eq. (11) is the zero range knock-on exchange contribution since the exchange is possible between the projectile and the target, $J_{00}(E)$ is linear energy dependent and can be expressed to account for the knock-out exchange term as [16]

$$J_{00}(E) = -276\,[1 - 0.005E/A_P]\ \text{MeV fm}^3, \quad (12)$$

where E is the laboratory energy of the projectile.

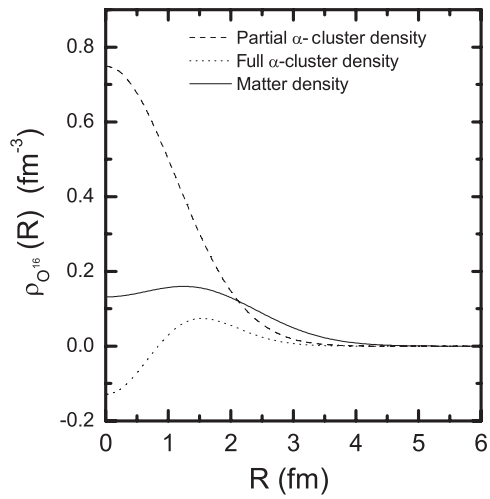

FIG. 1. A comparison among the partial α-cluster density (dashed line), full α-cluster density for ^{16}O (dotted line), and nuclear matter density distribution (sold line).

TABLE I. Density parameters used in Eqs. (13), (14), and (16) and the corresponding rms radii [22].

Nucleus	$\rho_{0(m,\alpha,C)}$ (fm^{-3})	w (γ) (fm^{-2})	$\beta(\lambda)$ (ξ) (fm^{-2})	rms radius (fm)
$\rho_m(r)$	0.1317	0.6457	0.3228	2.64
$\rho_\alpha(r)$	0.4229	0	0.7024	1.460
$\rho_C(r)$	−0.1286	−1.4249	0.5973	2.199

C. Density distributions

First, we consider the cluster structure $^{16}\mathrm{O} \equiv 4\alpha$. The matter density of the ^{16}O nucleus usually is expressed in a modified form of the Gaussian shape as [17,27]

$$\rho_m(r) = \rho_{0m}(1 + wr^2)\exp(-\beta r^2). \tag{13}$$

The matter density of the α particle also can be obtained in the Gaussian form as [17,27]

$$\rho_\alpha(r) = \rho_{0\alpha}\exp(-\lambda r^2). \tag{14}$$

The parameters $\rho_{0(m,\alpha)}$, ρ_{0M}, w, β, and λ and the corresponding root-mean-square (rms) radii are given in Table I. Now, if $\rho_C(r')$ is the α-cluster distribution function inside the ^{16}O nucleus, then we can relate the nuclear matter density distribution functions (13) and (14) as [17,27]

$$\rho_m(r) = \int \rho_C(r')\rho_\alpha(|\vec{r} - \vec{r}'|)d\vec{r}'. \tag{15}$$

Then, using Fourier-transform techniques [37] for expression (15), we can obtain

$$\rho_C(r') = \rho_{0C}(1 + \gamma r'^2)\exp(-\xi r'^2), \tag{16}$$

where $\xi = \frac{\beta\lambda}{\eta}$, $\eta = \lambda - \beta$, and $\gamma = \frac{2w\lambda^2}{[\eta(2\eta - 3w)]}$.

The ρ_{0C}, γ, and ξ parameters used in Eq. (16) are also listed in Table I. From this table, it is evident that the values for the α-cluster density in the ^{16}O nucleus are negative near the origin, i.e., at $r \leqslant 0.8$ fm as reported in Refs. [27,38]. The negative density discrepancy was also obtained previously during the analysis of pion-carbon elastic-scattering data by using the 3α-cluster model for the structure of the ^{12}C nucleus [39]. Inopin and Tishchenko [40] suggested that, perhaps, the size of the α particle is slightly changed inside the nucleus and that the zero is displaced to just outside the measured region. This may be cured by involving a correction term that depends on the rms radius of the α particle inside the nucleus. On the other hand, in Ref. [41], the α-cluster model that involved dispersion was proposed for the carbon and oxygen nuclei. In this approximation, it is assumed that the carbon and oxygen nuclei consist of three and four α-particle clusters located at the vertices of an equilateral triangle and a regular tetrahedron,

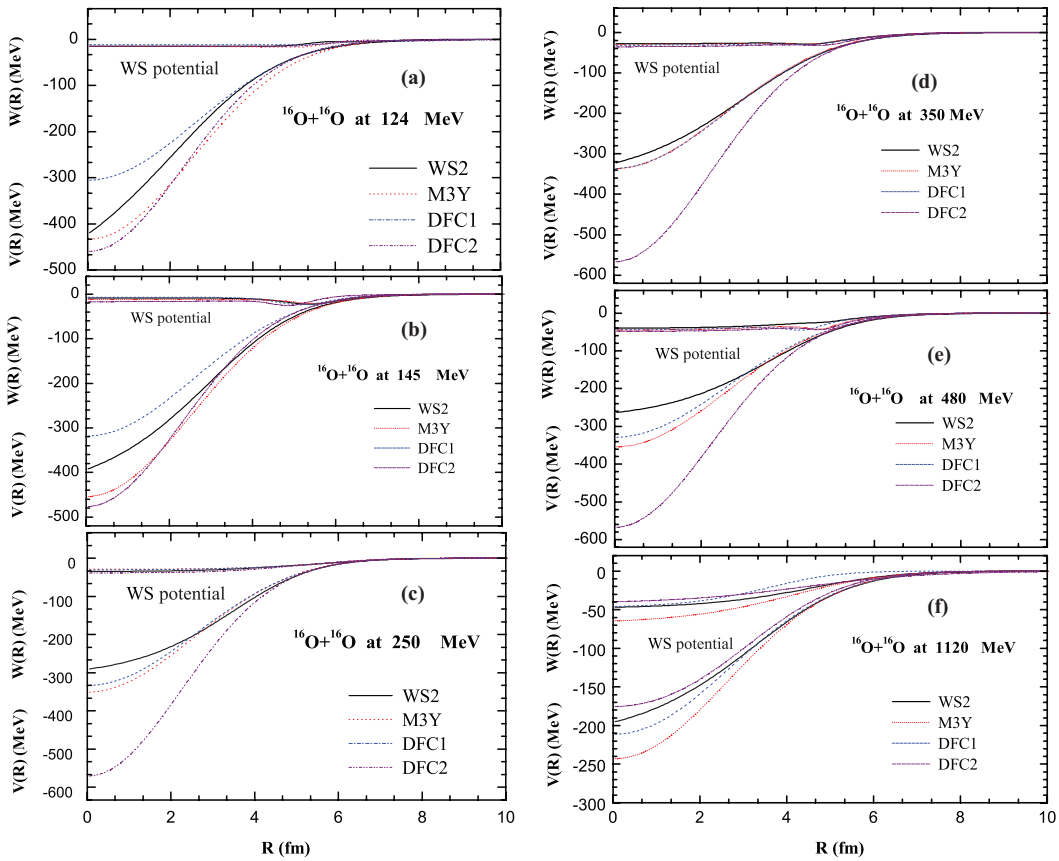

FIG. 2. (Color online) The comparison of the radial shapes of the real microscopic nuclear potentials (WS2, M3Y, DFC1, and DFC2) and the volume plus the surface (WS2 + WD) imaginary potentials used in our calculation at different energies.

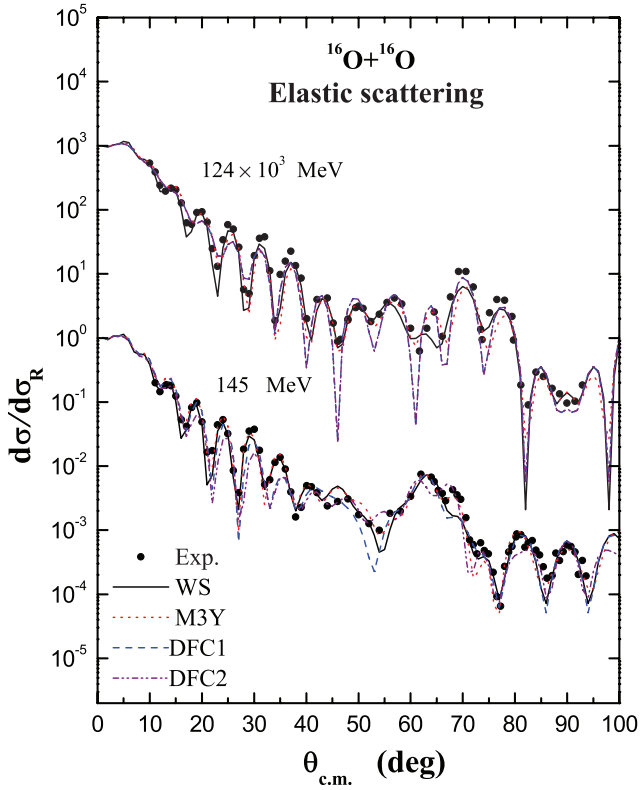

FIG. 3. (Color online) The predicted elastic differential cross sections relative to Rutherford scattering of the ^{16}O + ^{16}O reaction obtained by using the WS2, M3Y, DFC1, and DFC2 potentials at energies of 124 and 145 MeV in comparison with the data. Data are taken from Refs. [12,13,22].

respectively. These α-particle clusters can execute vibrations with respect to their most probable equilibrium positions at the vertices of the above geometric bodies. Owing to the small number of α clusters inside the ^{12}C and ^{16}O nuclei, which are distributed over these vertices, it is not expected to find α clusters close to the center of the nucleus such that this problem disappeared for the other nuclei when the number of α clusters was increased [38].

Now, we assume the cluster structure of ^{16}O as $^{16}\text{O} \equiv A_\alpha\alpha + \text{A}_N N$. The density distributions of the α clusters and unclustered nucleons in ^{16}O are taken to be of the modified Gaussian form as [26,27]

$$\rho_{iC}(r) = \rho_{0i}(1 + w_i r^2)\exp(-\beta_i r^2), \tag{17}$$

where $i = \alpha, N$. Since the ^{16}O nucleus is composed of A_α α particles plus A_N unclustered nucleons, we then have the normalization integral as

$$\int \rho_{\alpha C}(r)d\vec{r} + \int \rho_{NC}(r)d\vec{r} = 4A_\alpha + A_N = 16. \tag{18}$$

The considered values of the parameters are as follows: $\rho_{0\alpha} = 0.1667$, $\rho_{0N} = 0.082$ fm^{-3}, $w_\alpha = -0.035$, $w_N = -0.045$, $\beta_\alpha = 0.37$, and $\beta_N = 0.34$ fm^{-2}. These values yield $A_\alpha = 3.54$ and $A_N = 1.84$, and the corresponding rms radius of the ^{16}O nucleus equals 1.9 fm.

At the same time, we use the same nuclear matter density (13) in order to calculate the M3Y DF potential.

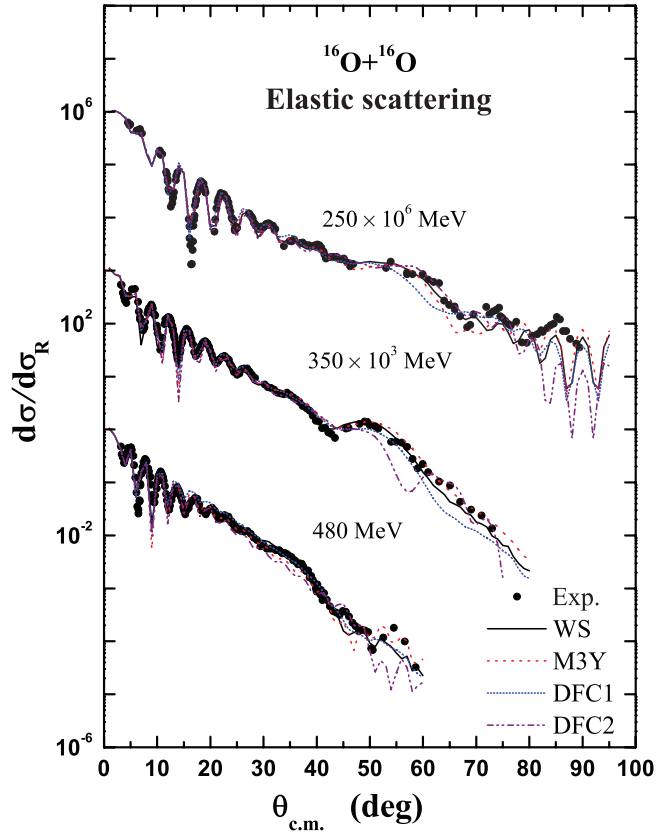

FIG. 4. (Color online) As Fig. 3 but at energies from 250 to 480 MeV. Data are taken from Ref. [13].

III. PROCEDURE

The present study is mainly devoted to the generation of semimicroscopic and microscopic descriptions of the real part of the ^{16}O + ^{16}O interaction. Therefore, as in previous analyses [30,42,43], we choose the imaginary part to be treated phenomenologically by using a conventional WS form. Thus, the total ^{16}O + ^{16}O potential is expressed as

$$U(R) = V_C(R) - N_R U_{\text{M3Y(DFC1,DFC2)}}(R) - iW_0[f_I(R)]^n - iW_D f_D(R). \tag{19}$$

All potentials obtained from our calculations, the real and WS2 + WD imaginary potentials, are shown in Fig. 2 at all considered energies, except for that at 704 MeV. All real potentials have the same strength and slope at the surface, which corresponds to the small overlap or low-density region. The main difference between different types of the folded potential is shown at short internuclear distances, which correspond to the higher overlap density of the colliding nuclei. In Fig. 2, we also notice that the DFC2 potentials are deeper than the WS2 ones, especially, at small radii, whereas, the other DF microscopic potentials reveal quite a resemblance to the WS2 potentials in the entire radial range at most considered energies. At the highest considered energy, 1120 MeV, the situation seems to be reversed where the other potentials are deeper than the WS2 ones. The corresponding imaginary potentials are weak and quite close to those found in Ref. [14], which clearly show the transparency of the optical potential

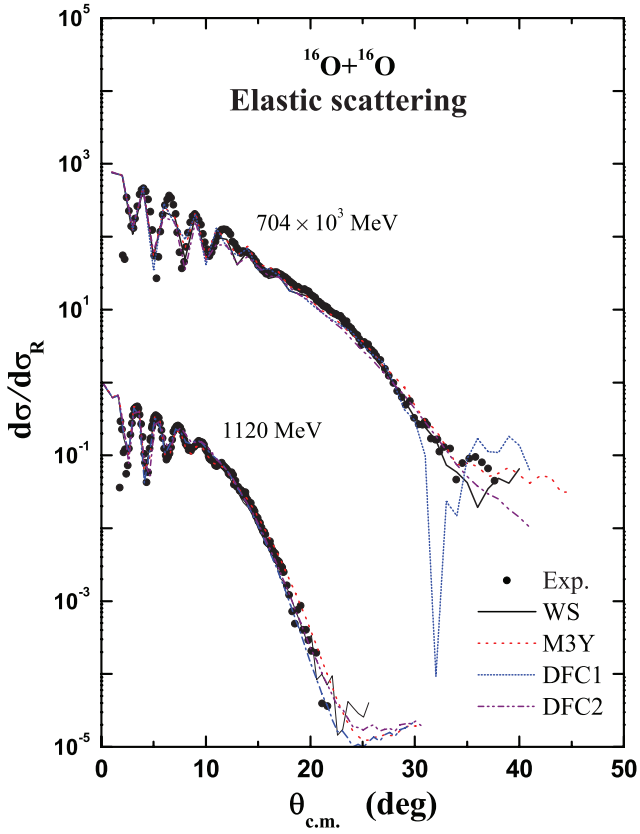

FIG. 5. (Color online) As Fig. 3 but at energies from 704 to 1120 MeV. Data are taken from Ref. [13].

for ^{16}O + ^{16}O at these energies. Thus, the discrepancy in the obtained cross sections at large angles is mainly due to the difference in the real folded potentials at the small internuclear distances to which the refractive cross section is particularly sensitive. In other words, this difference may cause improved folding model potential fits at forward angles where they give a correct account of the potential depth around the surface region to which the cross sections at forward angles are particularly sensitive as seen in Figs. 3–5.

The obtained potentials are fed into the computer codes HIOPTIM-94 [31] and HERMES [32] to calculate the angular distribution of elastic-scattering differential cross sections. The routine searches are carried out by considering an average value of 10% for all experimental data errors of the considered data to minimize the χ^2 value, which is defined as

$$\chi^2 = \frac{1}{N_D}\sum_{k=1}^{N_D}\left[\frac{\sigma_{th}(\theta_k) - \sigma_{\exp}(\theta_k)}{\Delta\sigma_{\exp}(\theta_k)}\right]^2, \qquad (20)$$

where N_D is the number of differential cross-sectional data points, $\sigma_{th}(\theta_k)$ is the calculated cross section at angle θ_k in the c.m. system, and $\sigma_{\exp}(\theta_k)$ and $\Delta\sigma_{\exp}(\theta_k)$ are the corresponding experimental cross section and its relative uncertainty, respectively. All potential parameters for M3Y, DFC1, and DFC2 are held constant during the search, except for the renormalization factor N_R and the depth of the real repulsive part of α-α interaction V_R together with the imaginary WS parameters, which are freely adjusted to fit the data by minimizing the χ^2 parameter.

IV. RESULTS AND DISCUSSION

In the present paper, seven sets of data for the angular distribution of the ^{16}O + ^{16}O elastic-scattering differential cross section at bombarding energies, which range from 124 to 1120 MeV are analyzed by using the constructed WS2, M3Y, DFC1, and DFC2 potentials. Best-fit parameters obtained for the real and imaginary potentials as well as the corresponding volume integrals per interacting nucleon pair J_R and J_I and reaction cross sections σ_R are listed in Tables II– IV. A comparison between the theoretical predictions and the corresponding experimental data are shown in Figs. 3–5. From these figures, it is clear that satisfactory descriptions of the data are obtained by using all considered potentials over all the angular measured ranges.

In phenomenological calculations, the real part of the optical potential is chosen in a WS2 form, whereas, a sum of WS or WS2 plus WSD terms has been used for the imaginary part for all considered energies. The Coulomb potential radius $R_C = 3.54$ fm is used for all calculations. The parameters of the phenomenological optical potential, used in the analysis, are given in Table II. This table reveals that the obtained potentials are constructed from deep real parts associated with rather shallow imaginary ones.

As mentioned above, the present study is mainly devoted to investigate the elastic ^{16}O + ^{16}O scattering by using two different real folded cluster potentials (DFC1 and DFC2). The

TABLE II. Best-fit phenomenological optical potential parameters. The real part is in a WS2 form, whereas, the imaginary part is a sum of WS or WS2 and WSD forms.

E (MeV)	V_0 (MeV)	r_V (fm)	a_V (fm)	W_0 (MeV)	r_I (fm)	a_I (fm)	W_D (MeV)	r_D (fm)	a_D (fm)	σ_R (mb)	χ^2
124	599.2	0.650	1.728	14.77	1.108	0.300	5.049	1.286	0.539	1708	9.9
145	448.9	0.790	1.480	8.77	1.365	0.833	16.010	1.076	0.435	1571	9.9
250	311.0	0.872	1.301	34.85	1.032	0.892	9.250	1.063	0.737	1745	8.3
350	367.1	0.801	1.480	28.15	1.266	1.000	8.426	0.921	0.344	1623	5.7
480	282.0	0.853	1.338	40.44	1.167	1.140	3.740	0.975	0.257	1567	5.3
704	294.8	0.836	1.409	41.98	1.197	0.990	2.481	0.921	0.265	1504	167
1120	219.0	0.852	1.503	48.41	1.100	1.346				1487	152

TABLE III. Microscopic potential. The real part is the folded (cluster folded) potential times N_R (V_R), and the imaginary part is the sum of a WS (WS2) and a WSD (WS2D) term used analysis of the elastic ^{16}O + ^{16}O data at energies of 124–1120 MeV.

Potential	E (MeV)	V_R (MeV)	W_0 (MeV)	r_I (fm)	a_I (fm)	W_D (MeV)	r_D (fm)	a_D (fm)	σ_R (mb)	χ^2
M3Y[a]		0.92	15.01	1.132	0.242	3.840	1.227	0.843	1916	13.9
DFC1[c]	124	58.0	11.33	1.203	0.278	4.150	1.483	0.725	2181	17.3
DFC2[c]		92.0	14.86	1.156	0.302	2.756	1.581	0.687	2347	14.3
M3Y[a]		0.97	12.10	1.258	0.545	10.777	1.099	0.354	1584	11.0
DFC1[c]	145	53.5	6.73	1.244	0.655	17.986	1.033	0.442	1570	14.2
DFC2[c]		85.0	16.785	0.974	1.200	16.986	0.976	0.325	2006	16.4
M3Y[b]		0.77	29.19	1.119	0.916	6.278	1.088	0.751	1723	9.6
DFC1[d]	250	48.5	30.69	1.111	0.972	6.443	1.085	0.747	1735	14.7
DFC2[d]		57.0	38.69	1.048	0.856	7.426	1.097	0.765	1782	10.5
M3Y[b]		0.76	29.70	1.244	1.020	7.630	0.917	0.321	1595	8.3
DFC1[d]	350	47.5	31.74	1.244	1.020	7.630	0.917	0.321	1618	7.2
DFC2[d]		58.0	35.70	1.212	1.043	10.70	0.972	0.342	1599	10.5
M3Y[b]		0.83	45.47	1.169	1.093	17.348	0.950	0.248	1581	8.9
DFC1[d]	480	50.0	44.47	1.158	1.111	17.219	0.867	0.278	1565	12.0
DFC2[d]		58.0	48.46	1.180	0.978	15.348	0.957	0.242	1541	9.8
M3Y[b]		0.81	51.44	1.164	1.031	14.631	0.823	0.222	1517	176.0
DFC1[d]	704	50.0	45.44	1.203	1.004	10.165	0.911	0.213	1550	176.0
DFC2[d]		104.0	66.49	1.049	0.823	10.610	1.049	0.823	1603	170.2
M3Y[b]		0.70	67.96	1.027	1.405				1498	191.2
DFC1[c]	1120	90.0	47.41	0.861	1.045				1654	152.0
DFC2[c]		175.0	41.74	0.861	1.045				1585	174.2

[a] N_R for the folding potential and the imaginary potential (WS + WSD).
[b] N_R for the folding potential and the imaginary potential (WS2 + WSD).
[c] $V_R = N_R$ for the folding cluster potential and the imaginary potential (WS + WSD).
[d] $V_R = N_R$ for the folding cluster potential and the imaginary potential (WS2 + WSD).

considered energy range is divided into two categories. The first category includes two low energies, 124 and 145 MeV. At these energies, the standard WS volume term plus the WSD surface term are used for the imaginary part. The second one belongs to energies from 250 to 1120 MeV at which the real DF potentials are supplemented with imaginary parts formulated from the sum of the WS2 and WSD terms. No renormalization of the two real cluster folded potentials is required to fit the data. From Fig. 3, it is observed that, at all considered energies, the DFC1 and DFC2 potentials produce almost similar predictions. However, one may notice that by introducing the treatment of unclustered nucleons in the structure of ^{16}O through the DFC2 potential relatively reduces the amplitude of oscillations in the predicted angular distributions, especially, at 124 and 145 MeV. In other words, this treatment yields slight improvement in fits with data, particularly, at forward- and middle-scattering angles. We recall that, at these low energies (<10 MeV/nucleon), refractive effects are observed in the structure of scattering angular distributions (see Fig. 3).

For the sake of comparison, an additional analysis is performed by using the microscopic M3Y DF potential. The predictions of the M3Y DF potential are almost identical to those of the DFC1 and DFC2 ones as displayed in Figs. 3–5. The average value of the renormalization factorN_R, required for the M3Y DF potential to get fits with low-energy data

TABLE IV. The volume integral of the optical potentials used in the theoretical calculations for the phenomenological and the double folding analyses of the ^{16}O + ^{16}O reaction at energies between $E_{\rm lab}$ = 124 and 1120 MeV.

E (MeV)	$J_{R_{Ph}}$ (MeV fm^3)	$J_{R_{\rm DF}}$ (MeV fm^3)	$J_{R_{\rm DFC1}}$ (MeV fm^3)	$J_{R_{\rm DFC2}}$ (MeV fm^3)	$J_{I_{Ph}}$ (MeV fm^3)	$J_{I_{\rm DF}}$ (MeV fm^3)	$J_{I_{\rm DFC1}}$ (MeV fm^3)	$J_{I_{\rm DFC2}}$ (MeV fm^3)
124	335.02	376.56	284.8	336.30	59.36	72.16	65.01	73.50
145	362.60	396.47	294.7	344.96	76.70	77.56	73.29	76.50
250	316.28	308.13	305.8	393.40	99.08	92.16	93.90	104.3
350	307.16	299.20	308.0	391.70	100.21	97.94	104.0	114.3
480	270.96	315.50	302.5	391.67	101.32	129.10	122.2	138.7
704	271.79	293.34	302.5	312.10	112.82	133.98	129.7	147.5
1120	217.09	225.69	214.2	190.97	96.48	111.24	99.72	92.10

equals ∼0.92, which is similar to that found in Ref. [12] at lower energies. Furthermore, our results, at 124 and 145 MeV, are similar, to some extent, to those obtained by the phenomenological potential and the DF one built upon the CDM3Y6 and α-α effective interactions [13,23], respectively. At the same time, the results obtained by all considered potentials are more successful to describe the scattering data than those found by phenomenological and DFC built upon an effective α-α-cluster interaction [22]. Furthermore, it is clear that the present predictions of 124-MeV data from all considered potentials are more successful than those yielded by the DF potential built upon the BDM3Y1 effective *NN* interaction [12]. Also, our results at 145 MeV are comparable to those found by El-Azab Farid *et al.* [19], which use the DFC potential based upon the pure attractive α-α-cluster effective interaction and the full α-cluster structure.

For energies between 250 and 1120 MeV, the data are successfully reproduced over all the measured angular ranges by using the two different real DFC1 and DFC2 without a renormalization factor. The renormalization factor N_R, required for the M3Y microscopic potentials to get fit to the data, is ranged as 0.7–0.85, which is similar to the result given in Ref. [13]. By comparing our results at higher energies with those obtained by previous studies, we find that the present fits with data are consistent, to some extent, with those obtained by the phenomenological potential and DF potential built upon the CDM3Y6 effective *NN* interaction [13]. At the same time, it is evident that the present predictions for the 250-, 350-, and 480-MeV data are more successful than those yielded by the DF and DFC potentials built upon the BDM3Y1, BDM3Y2, BDM3Y3, and α-α-cluster effective interactions [8,19,23].

The obtained values of real and imaginary volume integrals, listed in Table IV, are plotted against energy as shown in Fig. 6. From Table IV, it is evident that, at some considered energies, the real volume integrals $J_{R_{\mathrm{DFC2}}}$ of the DFC2 are significantly larger than those found from the other potentials. This behavior results from the large values of the repulsive depth V_R used in the calculations at lower energies, whereas, at the higher energies, this value decreases with increasing energy. The different behaviors of DFC1 and DFC2 result from the decrease in the ratio between the strength values where V_R (DFC2) / V_R (DFC1) < 2, but at 704 and 1120 MeV, this factor increases up to 2 and $J_{R_{\mathrm{DFC2}}}$ values are almost similar to those of the DFC1 potentials.

From Fig. 6(b), we see that J_R reveals linear energy dependence, whereas, J_R decreases as energy increases for all considered potentials. These results agree quit well with that deduced from earlier OM analyses of the elastic ^{16}O [13,22,23] scattering. From this discussion, we can conclude that the energy dependence of the real HI optical potential is predicted quite well by the two versions of the cluster folding model given in the present paper.

The energy dependence of the obtained imaginary volume integrals J_I of all considered imaginary potentials as shown in Fig. 6 are almost similar over all the investigated energy ranges. This behavior is attributed to the consistent values of the imaginary depth W_0 used with all considered potentials as shown in Tables II and III. From Fig. 6(a), we notice that J_I reveals linear

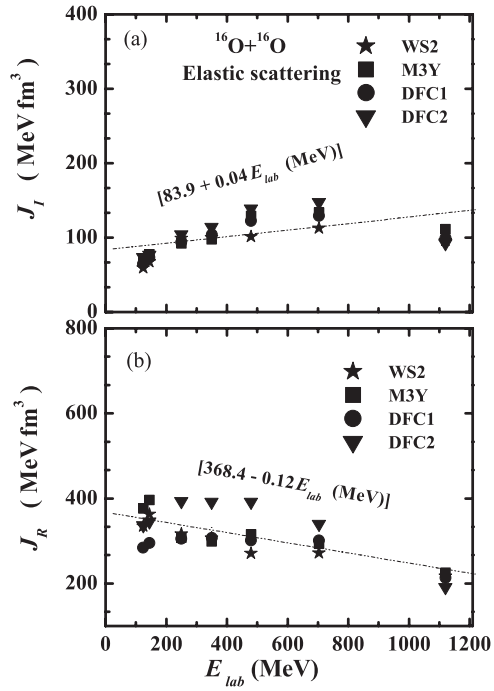

FIG. 6. Energy dependence of the real and imaginary volume integrals of the WS2, M3Y, DFC1, DFC2, and imaginary WS potentials.

energy dependence, whereas, J_I increases as energy increases for all considered potentials. We find $J_I = C + DE$, where $C = 84\pm7$ MeV and $D = 0.04$ for all considered potentials, i.e., the energies dependent in all potentials have slopes ≅0.04. On the other hand, the obtained J_I values are almost similar to those found by using the phenomenological and microscopic DF and DFC optical potentials based upon the CDM3Y6 [11–13], BDMEY1, DBM3Y2, BDM3Y3 [8], and α-α effective interactions [23].

The energy dependence of the reaction cross section σ_R is shown in Fig. 7. From Table III, it is clearly noticed that the results from all considered potentials are identical

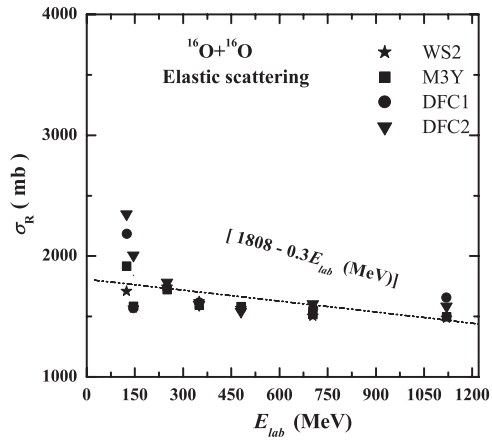

FIG. 7. Energy dependence of the total reaction cross sections deduced from the analysis of the ^{16}O + ^{16}O elastic scattering by using the WS2, M3Y, DFC1, and DFC2 potentials.

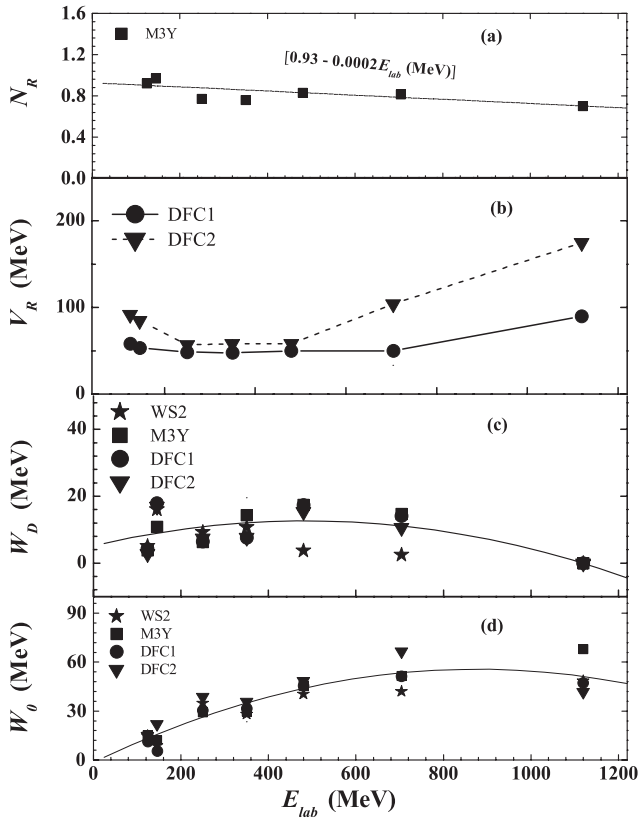

FIG. 8. The energy dependence of the best-fit parameters N_R, V_R, W_0, and W_D. Panels (a)–(d) show the results of energy dependence for the normalization coefficient N_R of the M3Y potential, the real repulsive depth of the α-α interaction in the DFC1 and DFC2 potentials, the derivative term of the imaginary potential, and the volume term of the imaginary potential supplemented with all real considered potentials, respectively. The solid and dashed lines are drawn as guides for the eyes.

except at 124 and 145 MeV where the DFC1 and DFC2 have greater values for σ_R than those of other potentials. Also, from Fig. 6, we notice that σ_R reveals a slight linear energy dependence, whereas, σ_R slightly decreases as energy increases for all considered potentials $\sigma_R = 1808$ and slopes $\sim$0.3. By comparing our values for σ_R with those obtained by previous studies, we find that the obtained σ_R's are consistent with those obtained by using the phenomenological [12,13] and microscopic DF potentials based upon the CDM3Y6 [11–13], BDMEY1, DBM3Y2, BDM3Y3 [8], and α-α effective interactions [23].

For completeness, the energy dependence of the best-fit parameters, N_R, V_R, W_0, and W_D are displayed in Fig. 8. From Fig. 8(a), one can see that the N_R factor for M3Y potentials has a negligible energy dependence and varies around a value of 0.93. From Fig. 8(b), we see that the real repulsive part of the α-α effective interaction V_R, used in both the DFC1 and the DFC2 potentials, does not show an explicit energy dependence. From Fig. 8(c), it is also obvious that the surface depth of the imaginary potential W_D is centered near 5–18 MeV to fit the data above 200 MeV; it decreases afterwards and becomes negligible beyond 1120 MeV. Also, from Fig. 8(d), it is obvious that the depth of the volume term W_0 is an increasing function of energy, whereas, its shape varies softly above 1120 MeV.

V. CONCLUSIONS

In the present paper, the angular distribution of the ^{16}O + ^{16}O elastic scattering at the bombarding energies ranging from 124 to 1120 MeV have theoretically been analyzed by using two types of the real double folding cluster optical potential. In the first one, the full α-cluster structure $^{16}\text{O} \equiv 4\alpha$ is considered. Then, the folded potential is calculated with the total contribution from the α-α attractive and repulsive effective interactions folded with the α-cluster density distribution inside projectile and target nuclei. However, in the second type, the cluster structure $^{16}\text{O} \equiv A_\alpha\alpha + A_N N$ is taken into account, and the potential is calculated from contributions of the α-α attractive and repulsive interactions besides the α-N and NN interactions, folded with the α-like cluster and unclustered nucleon density distributions in the colliding nuclei. The nuclear potential was constructed by a calculated real part supplemented with a phenomenological representation of the imaginary part.

Seven sets of ^{16}O + ^{16}O elastic-scattering data in the energy range of 124–1120 MeV are analyzed by using the derived potentials. The obtained results show that the successful description of the data over all the measured angular ranges can be obtained by using the constructed semimicroscopic potentials. It is shown that no renormalization of the real folded cluster potentials is required to fit the experimental data for all the considered energies. On the other hand, it is observed that, at all the considered energies, predictions produced by both potentials are almost similar. This may indicate that these data have very weak sensitivity to many-body correlations.

For the sake of comparison, two additional optical model potentials are constructed; one is microscopically designed based upon the M3Y interaction, and the other is phenomenologically represented. The success of the four derived potentials to describe the data is equivalent to that previously gained by using microscopic potentials based upon the DDM3Y1, BDM3Y1, BDM3Y2, and BDM3Y3 effective NN interactions.

Most of the obtained volume integrals and the extracted reaction cross sections are quite comparable to those obtained by previous studies by using phenomenological and microscopic potentials based upon the different versions of the density-dependent effective NN interactions. From these results, one may conclude that the energy dependence of the real HI optical potential is successfully predicted by the two considered versions of the cluster folding model.

Finally, it is worthwhile to point out that the present analysis shows an additional confirmation of the substantial ability of the α-cluster model to reproduce the measured elastic ^{16}O + ^{16}O scattering and reaction cross sections through the broad energy range of 8–70 MeV/nucleon.

[1] A. J. Cole, W. D. M. Rae, M. E. Brandan, A. Dacal, B. G. Harvey, R. Legrain, M. J. Murphy, and R. G. Stokstad, Phys. Rev. Lett. **47**, 1705 (1981).

[2] H. G. Bohlen, X. S. Chen, J. G. Cramer, P. Fröbrich, B. Gebauer, H. Lettau, A. Miczaika, W. von Oertzen, R. Ulrich, and T. Wilpert, Z. Phys. A **322**, 241 (1985).

[3] E. Stiliaris, H. G. Bohlen, P. Fröbrich, B. Gebauer, D. Kolbaur, W. von Oertzen, M. Wilpert, and T. Wilpert, Phys. Lett. B **233**, 291 (1989).

[4] A. M. Kobos, B. A. Brown, P. E. Hodgson, G. R. Satchler, and A. Budxanowski, Nucl. Phys. A **384**, 65 (1982); A. M. Kobos, B. A. Brown, P. E. Hodgson, R. Lindsay, and G. R. Satchler, *ibid.* **425**, 205 (1984).

[5] M. El-Azab Farid and G. R. Satchler, Nucl. Phys. A **438**, 525 (1985); **441**, 157 (1985).

[6] G. Bertsch, J. Borysowicz, H. McManus, and W. G. Love, Nucl. Phys. A **284**, 399 (1977).

[7] D. T. Khoa and W. von Oertzen, Phys. Lett. B **304**, 8 (1993).

[8] D. T. Khoa, W. von Oertzen, and H. G. Bohlen, Phys. Rev. C **49**, 1652 (1994).

[9] D. T. Khoa, W. von Oertzen, H. G. Bohlen, G. Bartnitzky, H. Clement, Y. Sugiyama, B. Gebauer, A. N. Ostrowski, T. Wilpert, and C. Langner, Phys. Rev. Lett. **74**, 34 (1995).

[10] G. Bartnitzky *et al.*, Phys. Lett. B **365**, 23 (1996).

[11] D. T. Khoa, G. R. Satchler, and W. von Oertzen, Phys. Rev. C **56**, 954 (1997).

[12] M. P. Nicoli, F. Haas, R. M. Freeman, N. Aissaoui, C. Beck, A. Elanique, R. Nouicer, A. Morsad, S. Szilner, Z. Basrak, M. E. Brandan, and G. R. Satchler, Phys. Rev. C **60**, 064608 (1999).

[13] D. T. Khoa, W. von Oertzen, H. G. Bohlen, and F. Nuoffer, Nucl. Phys. A **672**, 387 (2000).

[14] W. von Oertzen, A. Blazevic, H. G. Bohlen, D. T. Khoa, F. Nouffer, P. Roussel-Chomaz, W. Mittig, and J. M. Casandjian, Phys. At. Nucl. **65**, 678 (2002).

[15] D. T. Khoa, H. G. Bohlen, W. von Oertzen, G. Bartnitzky, A. Blazevic, F. Nouffer, B. Gebauer, W. Mittig, and P. Roussel-Chomaz, Nucl. Phys. A **759**, 3 (2005).

[16] B. Buck, C. B. Dover, and J. P. Vary, Phys. Rev. C **11**, 1803 (1975).

[17] Y. Goto and H. Horiuchi, Prog. Theor. Phys. **62**, 662 (1979).

[18] M. El-Azab Farid, J. Phys. G **16**, 461 (1990).

[19] M. El-Azab Farid, Z. M. M. Mahmoud, and G. S. Hassan, Nucl. Phys. A **691**, 671 (2001); Phys. Rev. C **64**, 014310 (2001).

[20] M. El-Azab Farid, Phys. Rev. C **65**, 067303 (2002); **74**, 064616 (2006).

[21] M. Karakoc and I. Boztosun, Phys. Rev. C **73**, 047601 (2006); Int. J. Mod. Phys. E **15**, 1317 (2006); G. Kocak, M. Karakoc, I. Boztosun, and B. Balantekin, Phys. Rev. C **81**, 024615 (2010).

[22] M. E. Kurkcuoglu, H. Aytekin, and I. Boztosun, Mod. Phys. Lett. A **21**, 2217 (2006).

[23] Y. X. Yang and Q. R. Li, Phys. Rev. C **72**, 054603 (2005).

[24] M. N. A. Abdullah, S. Hossain, M. S. I. Sarker, S. K. Das, A. S. B. Tariq, M. A. Uddin, A. K. Basak, S. Ali, H. M. Sen Gupta, and F. B. Malik, Eur. Phys. J. A **18**, 65 (2003).

[25] M. N. A. Abdullah, M. S. I. Sarker, S. Hossain, S. K. Das, A. S. B. Tariq, M. A. Uddin, A. S. Mondal, A. K. Basak, S. Ali, H. M. Sen Gupta, and F. B. Malik, Phys. Lett. B **571**, 45 (2003).

[26] S. Hossain, M. N. A. Abdullah, K. M. Hasan, M. Asaduzzaman, M. A. R. Akanda, S. K. Das, A. S. B. Tariq, M. A. Uddin, A. K. Basak, S. Ali, and F. B. Malik, Phys. Lett. B **636**, 248 (2006).

[27] M. A. Hassanain, A. A. Ibraheem, and M. El-Azab Farid, Phys. Rev. C **77**, 034601 (2008).

[28] M. A. Hassanain, Int. J. Mod. Phys. E **20**, 1931 (2011).

[29] M. A. Hassanain, Prog. Theor. Phys. **126**, 269 (2011).

[30] M. E. Brandan and G. R. Satchler, Phys. Rep. **285**, 143 (1997).

[31] N. M. Clarke (unpublished).

[32] J. Cook, Comput. Phys. Commun. **31**, 363 (1984).

[33] S. Ali and A. R. Bodmer, Nucl. Phys. **80**, 99 (1966); B. Buck, H. Friedrich, and C. Wheatley, Nucl. Phys. A **275**, 246 (1977).

[34] S. Sack, L. C. Biedenharn, and G. Breit, Phys. Rev. **93**, 321 (1954).

[35] M. El-Azab Farid and M. A. Hassanain, Nucl. Phys. A **678**, 39 (2000); **697**, 183 (2002); Eur. Phys. J. A **19**, 231 (2004).

[36] J. C. Pacheco, B. Bilwes, F. Sanchez, J. A. Ruiz, J. Diaz, J. L. Ferrero, and D. Kadi-Hanifi, Nucl. Phys. A **588**, 537 (1995).

[37] G. R. Satchler and W. G. Love, Phys. Rep. **55**, 183 (1979).

[38] Z. M. M. Mahmoud, M.Sc. thesis, Assiut University, 2000.

[39] J. F. Germond and C. Wilkin, Nucl. Phys. A **237**, 477 (1975).

[40] E. V. Inopin and B. I. Tishchenko, Sov. Phys. JETP **11**, 840 (1960).

[41] Y. A. Berezhnoy and V. P. Mikhailyuk, Phys. At. Nucl. **66**, 673 (2003); Y. A. Berezhnoy, V. P. Mikhailyuk, and V. V. Pilipenko, *ibid.* **68**, 940 (2005).

[42] G. R. Satchler and D. T. Khoa, Phys. Rev. C **55**, 285 (1997).

[43] M. E. Brandan and K. W. McVoy, Phys. Rev. C **55**, 1362 (1997).